3D reconstruction benchmark of a Compton camera against a parallel hole gamma-camera on ideal data

Yuemeng Feng, Ane Etxebeste, David Sarrut, Jean Michel Létang, Voichita Maxim

3D reconstruction benchmark of a Compton camera against a parallel hole gamma-camera on ideal data

Yuemeng Feng, Ane Etxebeste, David Sarrut, Jean Michel Létang, Voichiţa Maxim

***Abstract*—Compton cameras and collimated gamma cameras are competing devices suitable for prompt gamma detection in range verification of particle therapy. In this study, we evaluate the first approach from the point of view of the tomographic reconstruction step by comparing it to the second. We clear any technological constraints by considering a simple geometry, ideal detecting stages, a mono-energetic synthetic phantom. To this end, both analytic (filtered backprojection) and iterative (maximum likelihood expectation maximization) algorithms are applied in conjunction with total variation denoising. The results we obtain show that the collimated configuration leads to slightly better images when the same number of acquired events is used for the reconstruction. However, the Compton camera might equal the collimator-based camera if we take into account the superior efficiency and might surpass it in a limited angle configuration when the collimated camera cannot span the entire angular range.**

***Index Terms*—Compton camera imaging, gamma ray, maximum likelihood, maximum a posteriori, total variation**

I. Introduction

The Compton camera was proposed during 70's simultaneously for astronomical ([1]) and nuclear medicine ([2]) imaging applications. Several prototypes ([3], [4], [5], [6], [7]) have been built and exploited for the observation of cosmic γ sources, or for monitoring nuclear plants and waste with the development of hand-held γ-detectors boosted by the recent accident in Fukushima, Japan ([8], [9], [10], [11], [12]). Although Compton cameras should have superior efficiency ([13], [14], [15], [16], [17], [18], [19]), imaging of γ sources in nuclear medicine is still carried out with collimator-based gamma cameras. Compton cameras have recently regained interest as they may allow ion-range monitoring in proton and hadron-therapy using prompt-γ emission generated by nuclear interactions of the ions with tissue ([20], [21], [22], [23], [24], [25], [26], [27], [28]). The energies of the prompt-γ rays are too large to cope with parallel hole acquisition and requires hard collimation ([29], [30]). Three-dimensional imaging is then challenging, taking into account the low emission rates. To completely sample the projection space, multi-slit collimators combined with detectors rotating around the patient might be designed but would trigger significant burden.

The specificity of the Compton camera is to have a large acceptance angle and to identify the direction of an incoming ray without mechanical collimation, with a coincidence strategy based on Compton scattering followed by photoelectric absorption. However, the set of possible emission points can only be restricted to a conical surface unless the direction of the Compton electron is known, by contrast with the parallel hole geometry where the restriction to a line is possible. The analytic image reconstruction process is therefore relatively complex, reason for which analytic methods were initially available for subsets of data only: cone axis perpendicular to the detector in [31], point-like scatterer in [32], [33], two dimensions in [34]. Lately, methods accepting a much larger part of the data were developed ([35], [36], [37], [38]). The conical Radon transform is born and is receiving much interest ([39], [40], [41], [42], [43], [44], [45], [46]).

This conical projection pattern raises concerns about the quality that the reconstructed images can ever reach. Will it be possible, with both competitive detectors and reconstruction algorithms to obtain one day clinically acceptable images? Previous works attempted to benchmark the Compton camera with respect to the Anger camera from the point of view of detection efficiency and imaging capabilities. It is widely acknowledged that at energies superior to three or four hundreds of keV, Compton camera devices allow an increase in efficiency of one or two orders of magnitude ([47], [48]). Recently, a factor of 20 was found in simulations when compared the single particle emission computed tomography (SPECT) General Electric HealthCare Infinia system with a Compton camera prototype currently under development ([19]). These studies concentrate on the physical aspects and get rid as much as possible of the influence of one particular reconstruction algorithm. Our purpose is on the contrary to avoid as much as possible the influence of a particular geometry or physical effects and to concentrate on the image reconstruction capabilities, as function of the number of events. It is widely recognized that the Compton camera allows to sensibly increase the detection efficiency. One might wonder however if the more complex projection geometry and the supplementary degree of freedom due to conical surfaces is compatible with high quality images. In the final result, this supplementary degree of freedom could eventually completely cancel out the benefit of the superior efficiency. On the other side, Compton camera imaging can be done with a single stationary planar detector. This can be an advantage when the motion of the collimated camera is

The authors acknowledge financial support of the French National Research Agency through the ANR project 3DCLEAN (ANR-15-CE09-0009) and LABEX PRIMES (ANR-11-IDEX-0007) of Université de Lyon. This work was performed within the framework of the SIRIC LYriCAN Grant INCa_INSERM_DGOS_12563. The first author is supported by a PhD grant from the China Scholarship Council.

The authors are with Université de Lyon, INSA-Lyon, Université Claude Bernard Lyon 1, UJM-Saint Etienne, CNRS, Inserm, CREATIS UMR 5220, U1206, F69621, Villeurbanne, France, e-mail: {yuemeng.feng, ane.etxebeste, david.sarrut, jean-michel.letang, voichita.maxim}@creatis.insa-lyon.fr

Manuscript received March 1, 2019.

restricted by physical obstacles.

The purpose of this work was to investigate the limits of the "ideal" Compton camera imaging capabilities, with the best reconstruction algorithms available in our team. As reference for the 3D reconstruction benchmark we took the "ideal" Anger camera with parallel holes in a missing angle configuration. We put aside the efficiency of the cameras to focus on reconstruction issues: virtual experiments where a relatively low number of counts were considered, with the lower bound set to 2×10^4 measured events for the Compton camera and 2×10^3 measured events for the missing angle Anger camera.

The geometry of acquisition as well as data selection and pre-processing strategies have a major impact on the resulting Compton camera images (see *e.g.*, [49], [14], [22], [50], [51], [27]). The spatial resolution of reconstruction can be improved by more accurate modeling of the physical effects ([52], [53] [54], [55]) and by deconvolution methods in data space for energy spectrum ([56]) or in spatial domain ([57], [58]). Imaging performance of conventional collimated Anger camera systems is primarily determined by properties of the collimator. At energies above 300 keV, the collimator septal thickness must be increased to reduce penetration and scattering at the price of a reduced sensitivity. The choice of the hole diameter is thus a trade-off between sensitivity and resolution. On the opposite side, the Compton camera resolution increases with the energy as the Doppler broadening and detector noise decrease. However, as the energy increases above 1 MeV, the probabilities for multiple interactions, pair productions and electron escape increase, too. This may lead to false coincidences and requires specific algorithms for the identification of the interaction sequence [59]. In this work, the energy of the γ-rays has no influence on the Anger camera data and images as the data are Poisson-realisations from ideal parallel-line projections. For the Compton camera, three energies were considered: 511 keV, 2 MeV and 4 MeV. This choice influences the result through the Klein-Nishina differential cross-section which gives the probability for the scattering angle value. At low energies as the ones currently used in SPECT, high scattering angles are dominant. As the energy increases, forward scattering prevails. In theory, this might have an influence on the missing-data artefacts. However, we deliberately chose here a large camera that limit as much as possible data truncation.

II. The two simulated setups

A. Compton camera (CC)

1) Device description: CCs detect the γ photons on the basis of a coincidence process. The photon needs to hit the camera twice: once in the scatterer stage, once in the absorber stage. The first interaction has to be a Compton scattering. During this inelastic interaction the photon transfers part of its incident energy to an electron as kinetic energy E_1, which is ideally totally released in the detector at V_1 (see figure 1). The scattered photon, deviated by scattering angle β, has to interact with the camera at least once again at some position V_2. The quantities of interest are the positions of the two first hits, the energy E_1 and the total energy of the photon, E_0, that can be estimated by summing up the energies deposited in sensitive material. The scattering angle β may be deduced through the Compton kinematics.

To achieve both high Compton-to-photoelectric interaction ratio and low Doppler broadening, materials with low-Z elements as Silicon are often chosen for the scatterer. At high energies, scattering detectors made with Ge ([60]), CZT ([61]), $LaBr_3$ ([62]) might be preferred to reach a high efficiency of detection. Meanwhile the Doppler broadening will be increased and the Compton-to-photoelectric ratio will be reduced ([63]), which leads to a more noisy dataset for imaging. Several layers of scatterer can be ranged in a stack and the furthest detector use to be made of scintillating crystals, similar to the detector of the Anger camera. Its role is to completely stop the photon by photoelectric absorption, which have given it its name of absorber (see figure 1).

In the absence of noise, the point where the gamma ray was emitted lies on the surface of the cone having its apex at the first interaction, its axis directed by the line defined by the first two interactions and its half-opening angle β. As a consequence, data acquired with a CC having ideal position and energy resolutions are usually modelled as integrals of the weighted intensity of the source on conical surfaces. These models are gathered under the name of weighted conical Radon transforms, cone transforms or Compton transforms.

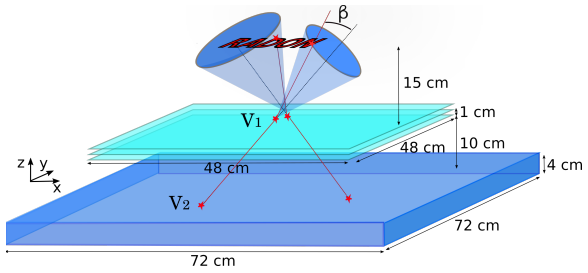

Fig. 1. Schematic representation of a CC composed of a three-layer scatterer (light blue) and an absorber (dark blue). The source is represented as the word RADON. Photons emitted from the source are first scattered then absorbed in the detector, and the position where they were emitted can only be determined at this stage as belonging to conical surfaces. The scattering and absorption positions are respectively noted V_1 and V_2. The scattering angle is noted β.

2) Monte Carlo simulated data: Each Compton cone is characterised by the coordinates of the apex, the two angular coordinates of the axis and the half-opening angle. The dimension of the data space is thus 5 or 6, and simulation of deterministic conical projections on a sufficiently fine grid is prohibitive. Moreover, for e.g. 10^5 counts, most of the projections would be empty. Thus, Monte Carlo data have to be produced event by event.

A new GATE ([64]) CC module currently under development at CREATIS, France ([65]) was used for simulations. The simulated Compton camera is shown in figure 1. The scatterer detector was composed of three parallel silicon layers with $48 \times 48 \times 0.2$ cm^3 in size separated by 1 cm distance from each other. The absorber was made of a $72.96 \times 72.96 \times 4$ cm^3 $LaBr_3$ pixelated scintillator matrix composed of 128×128 pixels with $0.5 \times 0.5 \times 4$ cm^3 in size. The distance between

the last silicon layer (center) and the center of the absorber was 10 cm. The source was placed parallel to the camera at a distance of 15 cm from the first scatterer layer. All the coincidences with at least one interaction in each detector type (scatterer and absorber) were accepted. In order to recover the ideal Compton kinematics, the positions of the first two primary interactions were stored together with the initial energy and the energy of the first Compton scattered photon. In addition, the *option 1* of the standard electromagnetic physics list, which does not include Doppler broadening, was activated.

B. Anger camera (AC)

1) Device description: To be detected by the AC, a γ photon emitted by the source must pass through a hole of the collimator then interact with the sensitive material. Usually, the detection is based on photoelectric absorption of the photon in a scintillating crystal, followed by measurement of visible light. The efficiency of the system is relatively low, as a fraction of photons hits the collimators and are either absorbed or scattered. The scattered photons, whose incoming direction is uncertain, are discarded on the basis of their lower energy. ACs are usually designed for relatively low energies, in the order of tenths until few hundreds of keV. For higher energies, collimators need to be thicker and significantly reduce the efficiency. For instance, knife-edge ([29]) and slit ([30]) cameras were proposed for the detection of the prompt-γ emission that has an energy spectrum going up to a few MeVs. This type of detector provides a 1D signal that might be sufficient for on-line range monitoring purposes. However, 3D images would give more extensive information on the irradiated area and even on the tissue composition.

2) Simulated data: In this work we do not deal with issues related to collimators. Parallel line projections were taken for each YZ slice from the source with the `radon` function from Matlab. The spacing between the centres of two adjacent holes was 0.25 cm, the same as the thickness of a slice, and the angular step was 6°. The energy of the source was not taken into account. From these deterministic exact projections, Poisson measures were then simulated. The total number of counts was a random number with given mean. This mean will be loosely referred in the text as the number of counts, as the small variation of its value do not significantly affect the results. The AC turns around the x axis as indicated in figure 3 with the green arrow. At 90° the camera is perpendicular to the z axis. We considered a limited angle configuration [30,150] degrees, for a total angle of 120° and a missing angle of 60°. The choice of the missing angle value was motivated by the similar missing angle in the Compton camera configuration, where the solid angle covered by the first scatterer layer at the center of the source, in the plane yOz, was slightly less than 120°. We neglect the loss of data in the plane xOz, despite the fact that this loss will have the most severe consequences, especially at the extremities of the source.

C. The source

We simulated a mono-energetic source consisting of five letters with thickness 1 cm. The source is composed of four slices with thickness 0.25 cm each, identical to the one shown in figure 2, the coordinates represent centimetres. The intensity is piecewise constant in each letter, as they are composed of boxes and parts of hollow cylinders. For instance, the letter "O" can be seen as a source containing two hot inserts and one cold insert. For the Compton camera simulations, the isotropic source was let to emit photons at three energies, 511 keV, 2 MeV and 4 MeV respectively. For the AC, the energy was not modelled in the simulation.

Fig. 2. Central slice from the simulated source.

Three placements of the source were considered, all shown in figure 3. The center of the volume is at the center of the coordinate system and thus at 15 cm from the Compton camera. The distance to the AC is not modeled.

With the TV-MAP-EM algorithm described hereafter, we reconstructed images from 2×10^4, 2×10^5 and 2×10^6 counts. For the CC analytic algorithm more events were necessary. From 25×10^6 simulated events, only one half were usable as a valid Compton cone should not intersect the detector in more than one point, the apex (for details, see reference [45]). A number of 12.5×10^6 counts were then simulated for the Anger camera with limited angular coverage.

III. Image reconstruction methods

The image of the source can be reconstructed from the measured data either analytically, with a filtered backprojection algorithm, or by iterative algorithms. Among iterative algorithms, the most widely employed is the maximum likelihood expectation maximization algorithm (MLEM), common to all emission tomography modalities ([66], [67]) and formally described for general distributions in the seminal paper [68]. Its specificity lies in the proper modelling of the Poisson nature of the data and in providing positive solutions without the need of additional projection steps. MLEM has several variants,

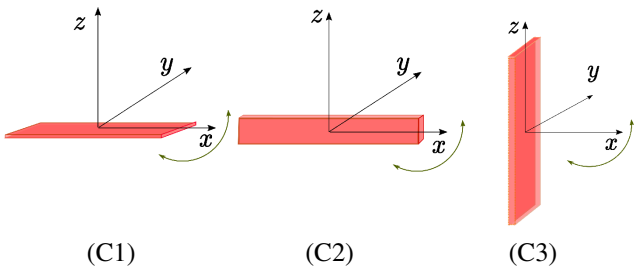

Fig. 3. Positions of the source, represented as a red rectangle. (C1) Source parallel to the camera allowing to evaluate the quality of the reconstruction for very thin extended sources. (C2) Source perpendicular to the camera, with effective length of about 20 cm and height 4 cm. (C3) High source, to evaluate the degradation of the quality of the images in the direction orthogonal to the Compton camera. The AC rotates around the x axis as indicated by the arrows.

among which OSEM ([69]) and list-mode MLEM ([70], [71]). When prior information on the solution is necessary to compensate for the low number of counts and to reduce the noise, maximum a posteriori (MAP) EM algorithms can be used.

A. Filtered backprojection

In this work, we applied the filtered backprojection algorithm developed for CC image reconstruction in [45]. It was shown in [31] that an infinitely large planar detector offers a complete geometry, and the source can be perfectly reconstructed even from only events corresponding to cones with axes perpendicular to that plane. A method allowing to consider arbitrary axis directions was proposed in [37], and the supplementary data is used for noise reduction. For each element of scatterer, the integrals of the source intensity on half-lines can be obtained from the set of conical projections composed of all possible axis directions and scattering angle in some interval $[\beta_1, \beta_2]$. At sufficiently high energy and thus for low scattering angles, most of these cones can be measured with a camera with scatterer as large as the source and a sufficiently large absorber. By letting the camera turn around the source, a complete set of cone-beam projections can thus be obtained. We do not chose this solution for several reasons. First, at low emission rates, very few events that scatter for the first time in a particular detector element will be measured. The computation of the cone-beam projections will be then compromised. Second, the cost of such a device would be high. Finally, our aim is to test a limited-scan geometry, where an AC could not complete a 180°-trip around the source, and thus 3D imaging with a CC covering a limited angle would be of interest. Some attempts to find a complete acquisition geometry and associated analytic reconstruction algorithms can be found in [35], [38], [43]. Similar to the missing angle parallel-ray acquisitions, any planar finite CC will lead to artefacts in the reconstructed images. These artefacts increase as the solid angle covered by the detector at the source position decreases. Prior to reconstruction, a sort of sinogram has to be completed by binning the data with respect to the coordinates of the cone apex, the axis angular parameters in spherical coordinates and the scattering angle β. The resulting array has five or six dimensions, depending on the number of scatterers of the camera. This binning reduces the precision on the data and the effect on the image can be remarkable. For instance, a systematic error of 2.5° on the axis inclination will alter the point spread function (PSF) as one moves far from the detector ([45], Fig. 7). The same error on the scattering angle will additionally cause displacement of the source and even prevent reconstruction. These results were obtained with the MLEM algorithm (in its classical variant, not in list-mode), from deterministic projections and perfect knowledge of the system matrix.

For the collimated camera, filtered backprojection implemented in Matlab as the `iradon` function was applied to each slice of the volume.

When the images were reconstructed by filtered backprojection, a smoothing filter was always applied in order to counterbalance the ramp filter at the higher frequencies and thus reduce the noise. These filters smooth the image and blur the edges. Total variation denoising ([72]) might be better suited at least for piecewise constant images. We therefore applied the total variation denoising method from [72], implemented following [73]. The analytic methods are fast, but work properly only for high number of counts where, in addition, list-mode MLEM algorithms exhibit prohibitive computing times. For this reason, we have only shown the analytic reconstruction results in the experiment of high number of counts.

B. Maximum likelihood expectation maximization algorithm

Let t_{ij} denote the probability for a photon emitted in voxel j to be detected as event i and let λ_j be the mean number of photons emitted in voxel j. The number of photons detected by the i^{th} element of detector also follows a Poisson law, with mean $\mu_i = \sum_j t_{ij}\lambda_j$. Note that for the CC, the index j has to account not only for positions, as it is the case for the Anger camera, but also for the polar and azimuthal angles of the axis of the cone and for the Compton scattering angle. The reconstruction problem might be seen as a linear inverse problem,

$$\boldsymbol{\mu} = T\boldsymbol{\lambda}, \tag{1}$$

where $\boldsymbol{\lambda}$ has positive values and the measured vector $\boldsymbol{y}$ follows a Poisson distribution with mean $\boldsymbol{\mu}$. The matrix $T = (t_{ij})$ is often called system matrix. The logarithm of the likelihood of a measurement $\boldsymbol{y}$ generated from the emission $\boldsymbol{\lambda}$ can be formulated as:

$$L(\boldsymbol{\lambda}|\boldsymbol{y}) = \sum_i (-\sum_j t_{ij}\lambda_j + y_i \ln(\sum_j t_{ij}\lambda_j) - \ln(y_i!)) \tag{2}$$

Let $s = (s_j)$ be the sensitivity vector, containing the detection probabilities for photons emitted from voxels j. The MLEM algorithm consisting to calculate, starting from some initial value $\widehat{\boldsymbol{\lambda}}^0 \in (\mathbb{R}_+^*)^J$, the sequence

$$\widehat{\lambda}_j^{l+1} = \frac{\widehat{\lambda}_j^l}{s_j} \sum_i \frac{t_{ij} y_i}{\sum_k t_{ik} \widehat{\lambda}_k^l}, \tag{3}$$

solves the minimization problem:

$$\min\{-L(\boldsymbol{\lambda}|\boldsymbol{y}) \,:\, \boldsymbol{\lambda} \in (\mathbb{R}_+)^J\}. \tag{4}$$

In the list-mode version, the data space is highly sampled in order to have $y_i \in \{0, 1\}$. The main differences are that each measured event becomes a "bin", only non-empty bins are used in the reconstruction, and the sensitivity calculation changes. The sensitivity is related to the system matrix through the relation $s_j = \sum_i t_{ij}$. In list-mode, the sampling of the data space is huge, therefore only the elements corresponding to measured events are calculated for the system matrix. Consequently a different strategy has to be employed for the calculation of the sensitivity. List-mode is indispensable for CC imaging for at least three reasons. First, the huge dimension of the data space (indexed on five or six parameters) that would require huge storage capacities or coarse sampling in each direction. Second, the CC is expected to

make the difference in conditions where the number of counts is relatively low. Regarding the first argument, it is likely that the number of events should be lower than the number of bins for reasonable sampling rates. Third, sampling induces some reduction in the precision of the data. This reduction does not excessively penalize modalities where the acquisition is made on lines, but even mild errors on the angular parameters have significant consequences on the reconstructed images of the CC (see discussion in section III-A).

MLEM algorithm was used for the first time for Compton camera imaging in [71]. Currently there is no established model for the calculation of the system matrix, but several proposals have been made in the literature ([74], [75], [76]). In [24], a MLEM based reconstruction framework together with an imaging prototype were presented and the proposed system matrix was tested on measured data. Monte Carlo simulations can help to choose and validate a model, but probably only up to some approximations induced by data binning. We used the approach detailed in [52], where it was demonstrated that the elements of the system matrix can be approximated up to a constant factor as

$$t_{ij} = \int_{M \in v_j} K(\beta_M, E_0) \frac{\cos \theta_{\overrightarrow{V_1 M}}}{\|\overrightarrow{V_1 M}\|^2} h_i(M) dv, \qquad (5)$$

where $K(\beta_M, E_0)$ is the Klein-Nishina Compton scattering cross-section ([77]), M is a point in the voxel v_j, $\theta_{\overrightarrow{V_1 M}}$ is the angle made by $\overrightarrow{V_1 M}$ with the axis of the camera and h_i is a spatial kernel modelling the cone and the uncertainties on the Compton angle β. For ideal data, h_i is the Dirac distribution on the cone associated to the i^{th} event. For the calculation of the sensitivity we generalized the formula from [75] to several scatterers.

The statistical noise and sometimes the ill-conditioned nature of the problem may lead to significant noise in the reconstructed images. As a consequence, the iterations of the MLEM algorithm have to be stopped at some point that is difficult to anticipate and in clinical routine the images use to be post-smoothed. Choosing a post-smoothing filter is a key issue as the noise in the MLEM images is not uniform but spatially variant with standard-deviation depending on the intensity ([78], [79]).

A better choice, allowing a balance between the data fidelity constrain represented by the log-likelihood (2) and some a priori, consists in including both of them in a penalized optimization problem. The ML-EM algorithm becomes the maximum a posteriori or MAP-EM algorithm. The second is sometimes implemented as appropriate smoothing of the solution between each two iterations of the first. The positivity of the solution can be easily ensured and the relative fast convergence of MLEM is preserved and even reinforced. Maximum a posteriori method brings general information about the source that allows to search for the solution in a smaller space. Often some regularity of the intensity function is imposed. In this work, we applied a non-smooth and spatially variant penalty: the total variation norm of the solution. For strong noise, corresponding to low statistics, total variation might be a good choice for classes of images more general than the piecewise constant class ([80]).

C. Total variation prior

Adding total variation regularization to Poisson-distributed data tomography aims to reconstruct the image with both minimal total variation and maximal log-likelihood through the resolution of the minimization problem:

$$\min\{-L(\boldsymbol{\lambda}|\boldsymbol{y}) + \alpha G(\boldsymbol{\lambda}) : \boldsymbol{\lambda} \in (\mathbb{R}_+)^J\}. \qquad (6)$$

Here $\alpha \geq 0$ is the weight of TV regularization and G denotes the discrete version of the L_1-norm of the gradient in the image:

$$G(\lambda) = \int_\Omega |\nabla \lambda(x)| dx. \qquad (7)$$

We used the method proposed in [81] for solving the MAP-TV regularization problem within EM iterations. The method is based on the Fenchel-Rockafellar duality theorem and on the dual formulation of the (M) step from the EM algorithm. A fast iterative shrinkage-thresholding algorithm (FISTA) was used to speed up the convergence ([82]).

D. Figures of merit

To evaluate the reconstruction quality we calculated the structural similarity (SSIM) index between the reconstructed image and the reference normalized to their maximum of intensity ([83]). As the images were smoothed with the total variation prior, we expect a low variation for this maximum. Compared to peak signal to noise ratio (PSNR) and root mean square error (RMSE) which evaluate two images on a pixel-by-pixel basis, SSIM is closer to visual perception. However, it remains a global measure little affected by localized differences in the images.

IV. Results

In this section we evaluate with simulated data how the TV-MAP-EM reconstructed Compton camera images are affected by (A) the energy at which the source emits, (B) the number of acquired events and (C) the thickness of the source in the direction orthogonal to the camera. For (B) and (C) we perform a comparison with the Anger camera with coverage limited at 120°. A final test concerns high statistics experiments and analytic, filtered backprojection reconstruction. For both cameras, we reconstructed volumes having $121 \times 34 \times 34$ voxels for the (C1) and (C2) configurations. For the (C3) configuration, the volume has $34 \times 34 \times 113$ voxels, in order to avoid intersection between the volume and the CC. Each cubic voxel has 0.25^3 cm^3. The total volume is thus about $30 \times 8 \times 8$ cm^3 for the (C1) and (C2) configurations and $8 \times 8 \times 28$ cm^3 For each test, we show one of the two central slices of the word-shaped source (the word is composed originally of four slices).

A. Influence of the emission energy

In figure 4 we show the Compton camera images for the source emitting successively at energies 511 keV, 2 MeV and 4 MeV. The source was placed in configuration (C2) (see figure 3). We used 2×10^6 measured events for each reconstruction.

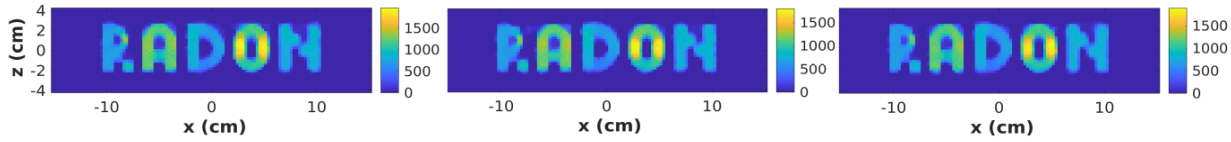

(a) 511 keV (b) 2 MeV (c) 4 MeV

Fig. 4. Images reconstructed from Compton camera data, as a function of the energy. From the left to the right the simulated energies are 511 keV, 2 MeV, 4MeV. The word-shaped source was placed perpendicular to the camera in configuration (C2). Central slices from the volumes reconstructed from 2×10^6 detected events at the 200th TV-MAP-EM iteration are shown.

B. Compton camera against limited angle Anger camera

The CC is expected to have an efficiency one or two orders of magnitude superior to the AC and to be used in applications where the counts are very low. The source, emitting at 511 keV, was placed perpendicular to the CC in configuration (C1). For the AC, at half-course the word is perpendicular to the detector. The AC is considered in a 120°-limited angle configuration. We then reconstructed the volumes for a number of detected events ranging from 2×10^4 to 2×10^6 for the CC and from 2×10^3 to 2×10^6 for the AC. The SSIM index comparing the reconstructed volumes to the reference image was calculated as function of the iteration number and plotted in figure 5.

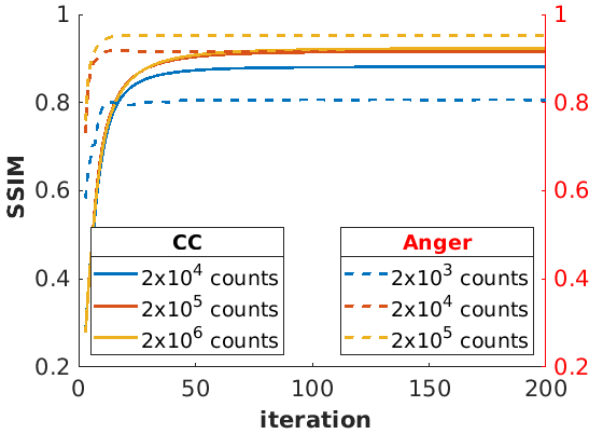

Fig. 5. Structural similarity between the reconstructed image and the reference. The images are normalized by their maximum.

Figure 6 compares the regularized iterative reconstructions from CC and AC for different counts. The image on the top-left is the reference. The results for the CC reconstruction are shown on the left side from the second line to the last, for respectively 2×10^6, 2×10^5 and 2×10^4 measured events. The results for the missing angle AC configuration with projections measured on 120° in the range [30°,150°] are shown on the right from the top to the end, for respectively 2×10^6, 2×10^5, 2×10^4 and 2×10^3 measured events.

C. Position of the source

The CC has lower resolution in the direction orthogonal to the detector. The position of the source also affects the AC images in a limited-angle configuration. In figure 7 we show the iterative reconstruction from 2×10^6 measured events for the three position (C1)-(C3) shown in figure 3. The source was let to emit at 511 keV and the result is shown at the 200th iteration for 2×10^6 measured events. Results for the CC and the AC are shown for comparison.

D. Analytic reconstruction from high counts

When the number of detected events is high, analytic reconstruction methods can be applied. Figure 8 compares filtered backprojection reconstructions from CC and from missing angle AC acquisitions, for 1.25×10^7 valid counts (see section II-C for details). TV-denoising was applied to the reconstructed volumes.

V. Discussions

The energy of the photons influence the shape of the Compton cones through the Klein-Nishina cross-section in CC imaging. At low energies, high scattering angles are favoured. As the energy increase, small angles related to almost forward scattering prevail. The data become then more and more close to the linear projection model. On the one hand, if the camera is small and is not let to turn around the source, missing angle artefacts would be expected. On the other hand, for large cameras an improvement could be expected as the surface of uncertainty decrease with the half-opening angle of the cone. From the results of the iterative reconstruction shown in figure 4, the influence of the energy on the image is not evident. The reason might be the large angular acceptance of the simulated geometry. These conclusions are not applicable to realistic data where the energy has a determinant influence on the results both for the CC (see for instance [50]) and the AC.

One conclusion that might be drawn from the comparison at different counts, is that at equal statistics, the AC is superior to the CC except for the missing angle artefacts that can be seen in the right column from figure 6. If we consider for the CC an efficiency ten times larger than for the AC, the images become visually comparable and even better for the CC as less affected by artefacts. As a rule of thumb, this factor of ten seems to be the price to pay when switching from linear to conical projections. We observed a factor somewhere between 10 and 100 for the full 180° with the AC. The second conclusion is that remarkably good images can be reconstructed from CC *ideal* data even at very low statistics. The shape of the source we considered is complex compared to point-sources, spheres or box sources, and the intensity is not uniform. The

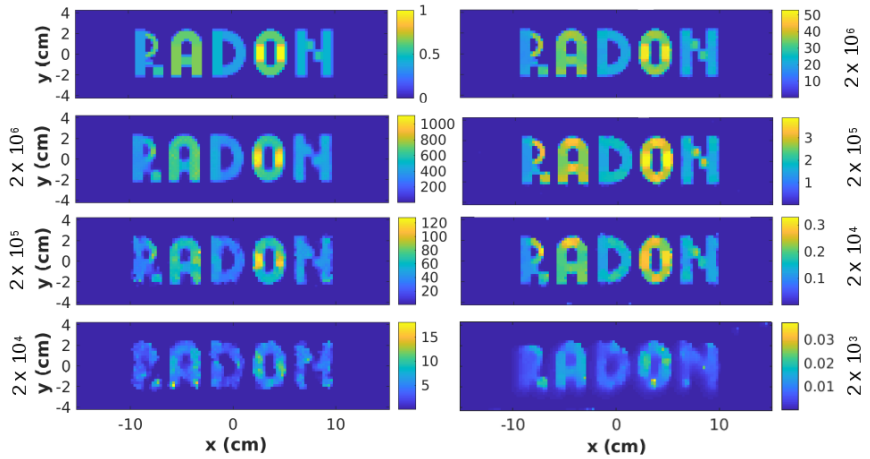

(a) Compton camera (b) Missing angle Anger camera

Fig. 6. Iterative reconstruction from Compton camera (left) and limited angle Anger camera (right) as a function of counts number. The simulated source was placed parallel to the camera and was emitted at 511 keV. Cuts in the center of x axis orthogonal to the y axes are shown at the 200th TV-MAP-EM iterations. **Add the number of events, vertically, on left and right**

shape of the letters is identifiable even with 2×10^4 detected events and the intensities are approximately well reproduced with 2×10^5 detected events. The third conclusion is that when comparing the SSIM indexes, the AC images seem more close to the original than the CC images, despite the missing angle artefacts that the eye can identify in the first ones.

As expected, the resolution degrades as one moves far from the camera in the orthogonal direction In figure 7, central slices for different positions of the source are compared. The differences between (C1) and (C2) are relatively mild. However, for the configuration (C3), the letter "N" is obviously blurred compared to the letter "R", which is placed 15 cm closer to the camera. This blur could be due to the finite extent of the camera and the resultant missing data, but also to some modelling imprecisions in the system matrix and in the sensitivity vector from (3). In real acquisitions, several factors further degrade image quality especially for distant sources. Detection uncertainties, due either to intrinsic Doppler broadening or to the detection process, can be at some extent be modelled in the system matrix and corrected for. Correcting for random coincidences, incomplete absorption and wrong sequencing of the hits can be more tricky. Furthermore, the uncertainties of the angular parameters, *i.e.*, Compton scattering angle and axis direction in spherical coordinates, will have severe consequences (for more details, see discussions in section III-A).

The reconstruction time of iterative methods become prohibitive for large CC data sets and analytic methods could be an alternative as they are much faster. With an optimal implementation, real time reconstruction could probably be reached. However, analytic methods cannot account for the detection model, for statistical noise and for the missing projections, giving less precise results. They still may give a coarse identification of the source, even with a number of counts much lower than the one considered here. It might be seen from the comparison that filtered backprojection gives poor results compared to iterative methods for both acquisition systems. Some artefacts that might be misleading for a quantitative evaluation of the images can be observed in the parallel missing angle acquisition. In comparison with Compton camera reconstruction in figure 6, figure 8 shows that the impact of missing data on analytic algorithms is higher than on iterative ones even at a number of detected events increased by a factor of more than 10. Binning could be another factor of degradation for Compton camera analytic reconstruction as it introduces errors on the measures. For a real Anger camera, the projections are not measured on straight lines as it was done here, the collimators allowing for some broadening. The influence of the binning for the collimated system cannot be measured in our set-up. Therefore the evaluation in real acquisition conditions needs to be further investigated.

VI. Conclusions

The aim of this work was to evaluate the imaging capabilities of the Compton camera independently of the detection technology, of the geometry or other factors that affect the results of a real detector. As reference we considered an ideal parallel hole collimated system. We investigated full-angle and missing-angle acquisitions for the collimated system, the latter reproduced the covering angle of the simulated Compton camera. In the full angle acquisition with the same number of counts the collimated system gave better quality reconstructed images. The Compton camera successfully competed against the missing angle collimated system in terms of uniformity in constant intensity regions in spite of a larger root mean squared error. Moreover, according to the literature an efficiency of detection 10-100 times higher is expected for Compton camera, which makes its application attractive for low dose and for missing angle acquisitions.

Generally, a list-mode MAP-EM reconstruction algorithm will give the best results. In particular, the missing angle geometry has a stronger impact on the images reconstructed by FBP compared to iterative algorithms. This can be seen

from the Anger camera images at high statistics. However, the much faster analytic filtered backprojection is an appealing alternative for Compton camera high statistics data.

Compton camera imaging may bring several improvements in nuclear medicine and provide clinically exploitable images. However, the results of this work cannot be extended directly to real detectors and clinical application. We can only infer that Compton cameras could be useful for configurations where a collimated detector cannot turn around the patient and thus missing angle data is generated. Besides, the advantage of Compton camera is more evident at high energies where the collimators become transparent, as it is the case in proton therapy.

REFERENCES

[1] M. Schönfelder, A. Hirner, and K. Schneider, "A telescope for soft gamma ray astronomy," *Nuclear Instruments and Methods*, vol. 107, no. 2, pp. 385–394, 1973.

[2] R. Todd, J. Nightingale, and D. Everett, "A proposed γ camera," *Nature*, vol. 251, pp. 132–134, 1974.

[3] V. Schönfelder, R. Diehl, G. Lichti, H. Steinle, B. Swanenburg, A. Deerenberg, H. Aarts, J. Lockwood, W. Webber, J. Macri *et al.*, "The imaging Compton telescope COMPTEL on the gamma ray observatory," *IEEE Transactions on Nuclear Science*, vol. 31, no. 1, pp. 766–770, 1984.

[4] S. M. Schindler, W. R. Cook, J. Hammond, F. A. Harrison, T. A. Prince, S. Wang, S. Corbel, and W. A. Heindl, "Grip-2: A sensitive balloon-borne imaging gamma-ray telescope," *Nucl. Instrum. Methods A*, vol. 384, no. 2-3, pp. 425–434, 1997.

[5] A. Zoglauer, M. Galloway, M. Amman, S. E. Boggs, J. S. Lee, P. N. Luke, L. Mihailescu, K. Vetter, and C. B. Wunderer, "First results of the high efficiency multi-mode imager HEMI," in *2009 IEEE Nuclear Science Symposium Conference Record (NSS/MIC)*. IEEE, 2009, pp. 887–891.

[6] M. Bandstra, E. Bellm, S. Boggs, D. Perez-Becker, A. Zoglauer, H.-K. Chang, J.-L. Chiu, J.-S. Liang, Y.-H. Chang, Z.-K. Liu *et al.*, "Detection and imaging of the Crab Nebula with the nuclear Compton telescope," *The Astrophysical Journal*, vol. 738, no. 1, p. 8, 2011.

[7] V. Tatischeff, M. Tavani, P. Von Ballmoos, L. Hanlon, U. Oberlack, A. Aboudan, A. Argan, D. Bernard, A. Brogna, A. Bulgarelli *et al.*, "The e-ASTROGAM gamma-ray space mission," in *Space Telescopes and Instrumentation 2016: Ultraviolet to Gamma Ray*, vol. 9905. International Society for Optics and Photonics, 2016, p. 99052N.

[8] L. Mihailescu, K. Vetter, M. Burks, E. Hull, and W. Craig, "SPEIR: a Ge Compton camera," *Nucl. Instrum. Methods A*, vol. 570, no. 1, pp. 89–100, 2007.

[9] J. Sullivan, S. Tornga, and M. Rawool-Sullivan, "Extended radiation source imaging with a prototype Compton imager," *Applied Radiation and Isotopes*, vol. 67, pp. 617–624, 2009.

[10] S. Takeda, A. Harayama, Y. Ichinohe, H. Odaka, S. Watanabe, T. Takahashi, H. Tajima, K. Genba, D. Matsuura, H. Ikebuchi, Y. Kuroda *et al.*, "A portable Si/CdTe Compton camera and its applications to the visualization of radioactive substances," *Nucl. Instrum. Methods A*, vol. 787, pp. 207–211, 2015.

[11] C. Wahl, W. Kaye, W. Wang, F. Zhang, J. Jaworski, A. King, Y. Boucher, and Z. He, "The Polaris-H imaging spectrometer," *Nucl. Instrum. Methods A*, vol. 784, pp. 377–381, 2015.

[12] A. Iltis, H. Snoussi, L. R. de Magalhaes, M. Hmissi, C. T. Zafiarifety, G. Z. Tadonkeng, and C. Morel, "Temporal imaging CeBr3 Compton camera: A new concept for nuclear decommissioning and nuclear waste management," in *EPJ Web of Conferences*, vol. 170. EDP Sciences, 2018, p. 06003.

[13] M. Singh and D. Doria, "An electronically collimated gamma camera for single photon emission computed tomography. Part II: Image reconstruction and preliminary experimental measurements," *Medical Physics*, vol. 10, no. 4, pp. 428–435, 1983.

[14] S. Takeda, H. Odaka, S. Ishikawa, S. Watanabe, H. Aono, T. Takahashi, Y. Kanayama, M. Hiromura, and S. Enomoto, "Demonstration of in-vivo multi-probe tracker based on a Si/CdTe semiconductor Compton camera," *IEEE Transactions on Nuclear Science*, vol. 59, no. 1, pp. 70–76, 2012.

[15] S. Motomura, Y. Kanayama, M. Hiromura, T. Fukuchi, T. Ida, H. Haba, Y. Watanabe, and S. Enomoto, "Improved imaging performance of a semiconductor Compton camera GREI makes for a new methodology to integrate bio-metal analysis and molecular imaging technology in living organisms," *J. Anal. At. Spectrom.*, vol. 28, pp. 934–939, 2013.

[16] J. Krimmer, J.-L. Ley, C. Abellan, J.-P. Cachemiche, L. Caponetto, X. Chen, M. Dahoumane, D. Dauvergne, N. Freud, B. Joly, D. Lambert, L. Lestand, J. Létang, M. Magne, H. Mathez, V. Maxim, G. Montarou, C. Morel, M. Pinto, C. Ray, V. Reithinger, E. Testa, and Y. Zoccarato, "Development of a Compton camera for medical applications based on silicon strip and scintillation detectors," *Nucl. Instrum. Methods A*, vol. 787, no. 0, pp. 98 – 101, 2015.

[17] G. Pausch, A. Schulz, and W. Enghard, "A novel scheme of Compton imaging for nuclear medicine," in *IEEE NSS-MIC conference*, 2016.

[18] A. Kishimoto, J. Kataoka, T. Taya, L. Tagawa, S. Mochizuki, S. Ohsuka, Y. Nagao, K. Kurita, M. Yamaguchi, N. Kawachi, K. Matsunaga, H. Ikeda, E. Shimosegawa, and J. Hatazawa, "First demonstration of multi-color 3-D in vivo imaging using ultra-compact Compton camera," *Scientific Reports*, vol. 7, 2017.

[19] M. Fontana, D. Dauvergne, J. Letang, J. Ley, and É.. Testa, "Compton camera study for high efficiency SPECT and benchmark with Anger system," *Physics in Medicine & Biology*, vol. 62, no. 23, p. 8794, 2017.

[20] M. Frandes, A. Zoglauer, V. Maxim, and R. Prost, "A tracking Compton-scattering imaging system for hadron therapy monitoring," *IEEE Transactions on Nuclear Science*, vol. 57, pp. 144–150, 2010.

[21] M.-H. Richard, M. Dahoumane, D. Dauvergne, M. De Rydt, G. Dedes, N. Freud, J. Krimmer, J. Létang, X. Lojacono, V. Maxim *et al.*, "Design study of the absorber detector of a Compton camera for on-line control in ion beam therapy," *IEEE Transactions on Nuclear Science*, vol. 59, no. 5, pp. 1850–1855, 2012.

[22] P. G. Ortega, I. Torres-Espallardo, F. Cerutti, A. Ferrari, J. E. Gillam, C. Lacasta, G. Llosà, J. F. Oliver, P. R. Sala, P. Solevi, and M. Rafecas, "Noise evaluation of Compton camera imaging for proton therapy," *Phys. Med. Biol.*, vol. 60, pp. 1845–63, 2015.

[23] T. Taya, J. Kataoka, A. Kishimoto, Y. Iwamoto, A. Koide, T. Nishio, S. Kabuki, and T. Inaniwa, "First demonstration of real-time gamma imaging by using a handheld Compton camera for particle therapy," *Nucl. Instrum. Methods A*, vol. 831, pp. 355–361, 2016.

[24] S. Schöne, W. Enghardt, F. Fiedler, C. Golnik, G. Pausch, H. Rohling, and T. Kormoll, "An image reconstruction framework and camera prototype aimed for Compton imaging for in-vivo dosimetry of therapeutic ion beams," *IEEE Trans. on Nuclear Science*, 2017.

[25] F. Hueso-Gonzalez, G. Pausch, J. Petzoldt, K. E. Roemer, and W. Enghardt, "Prompt gamma rays detected with a BGO block Compton camera reveal range deviations of therapeutic proton beams," *IEEE Trans. on Nuclear Science*, 2017.

[26] S. Aldawood, P. Thirolf, A. Miani, M. Böhmer, G. Dedes, R. Gernhäuser, C. Lang, S. Liprandi, L. Maier, T. Marinšek *et al.*, "Development of a Compton camera for prompt-gamma medical imaging," *Radiation Physics and Chemistry*, vol. 140, pp. 190–197, 2017.

[27] H. Rohling, M. Priegnitz, S. Schoene, A. Schumann, W. Enghardt, F. Hueso-González, G. Pausch, and F. Fiedler, "Requirements for a Compton camera for in vivo range verification of proton therapy," *Physics in Medicine and Biology*, vol. 62, no. 7, p. 2795–2811, 2017.

[28] J. Krimmer, D. Dauvergne, J. M. Létang, and É. Testa, "Prompt-gamma monitoring in hadrontherapy: A review," *Nucl. Instrum. Methods A*, vol. 878, pp. 58–73, 2018.

[29] M. Priegnitz, S. Barczyk, L. Nenoff, C. Golnik, I. Keitz, T. Werner, S. Mein, J. Smeets, F. V. Stappen, G. Janssens, L. Hotoiu, F. Fiedler, D. Prieels, W. Enghardt, G. Pausch, and C. Richter, "Towards clinical application: prompt gamma imaging of passively scattered proton fields with a knife-edge slit camera," *Physics in Medicine and Biology*, vol. 61, no. 22, p. 7881, 2016.

[30] J. Krimmer, M. Chevallier, J. Constanzo, D. Dauvergne, M. De Rydt, G. Dedes, N. Freud, P. Henriquet, C. La Tessa, J. M. Létang *et al.*, "Collimated prompt gamma TOF measurements with multi-slit multi-detector configurations," *Journal of Instrumentation*, vol. 10, no. 01, p. P01011, 2015.

[31] M. J. Cree and P. J. Bones, "Towards direct reconstruction from a gamma camera based on Compton scattering," *IEEE Transactions on Medical Imaging*, vol. 13, no. 2, pp. 398–407, 1994.

[32] L. Parra, "Reconstruction of cone-beam projections from Compton scattered data," *IEEE Transactions on Nuclear Science*, vol. 47, no. 4, pp. 1543–1550, 2000.

[33] T. Tomitani and M. Hirasawa, "Image reconstruction from limited angle Compton camera data," *Phys. Med. Biol.*, vol. 47, pp. 2129–2145, 2002.

[34] R. Basko, G. L. Zeng, and G. T. Gullberg, "Analytical reconstruction formula for one-dimensional compton camera," *IEEE Transactions on Nuclear Science*, vol. 44, no. 3, pp. 1342–1346, 1997.

[35] B. Smith, "Reconstruction methods and completeness conditions for two Compton data models," *J. Opt. Soc. Am. A*, vol. 22, pp. 445–459, March 2005.

[36] V. Maxim, M. Frandes, and R. Prost, "Analytical inversion of the Compton transform using the full set of available projections," *Inverse Problems*, vol. 25, no. 9, pp. 1–21, 2009.

[37] V. Maxim, "Filtered backprojection reconstruction and redundancy in Compton camera imaging," *IEEE Transactions on Image Processing*, vol. 23, no. 1, pp. 332–341, 2014.

[38] P. Kuchment and F. Terzioglu, "Inversion of weighted divergent beam and cone transforms," *Inverse Problems & Imaging*, vol. 11, no. 6, pp. 1071–1090, 2017.

[39] R. Gouia-Zarrad and G. Ambartsoumian, "Exact inversion of the conical Radon transform with a fixed opening angle," *Inverse Problems*, vol. 30, no. 4, p. 045007, 2014.

[40] M. Haltmeier, "Exact reconstruction formulas for a Radon transform over cones," *Inverse Problems*, vol. 30, no. 3, p. 035001, 2014.

[41] C.-Y. Jung and S. Moon, "Exact inversion of the cone transform arising in an application of a Compton camera consisting of line detectors," *SIAM Journal on Imaging Sciences*, vol. 9, no. 2, pp. 520–536, 2016.

[42] S. Moon, "Inversion of the conical Radon transform with vertices on a surface of revolution arising in an application of a Compton camera," *Inverse Problems*, vol. 33, no. 6, p. 065002, 2017.

[43] V. Palamodov, "Reconstruction from cone integral transforms," *Inverse Problems*, vol. 33, no. 10, p. 104001, 2017.

[44] D. Schiefeneder and M. Haltmeier, "The Radon transform over cones with vertices on the sphere and orthogonal axes," *SIAM Journal on Applied Mathematics*, vol. 77, no. 4, pp. 1335–1351, 2017.

[45] V. Maxim, "Enhancement of Compton camera images reconstructed by inversion of a conical Radon transform," *Inverse Problems*, vol. 35, no. 1, p. 014001, 2019.

[46] F. Terzioglu, "Some analytic properties of the cone transform," *Inverse Problems*, vol. 35, no. 3, 2019.

[47] J. E. Gormley, W. Rogers, N. Clinthorne, D. Wehe, and G. Knoll, "Experimental comparison of mechanical and electronic gamma-ray collimation," *Nucl. Instrum. Methods A*, vol. 397, no. 2-3, pp. 440–447, 1997.

[48] L. Han, W. L. Rogers, S. S. Huh, and N. Clinthorne, "Statistical performance evaluation and comparison of a Compton medical imaging system and a collimated Anger camera for higher energy photon imaging," *Physics in Medicine & Biology*, vol. 53, no. 24, p. 7029, 2008.

[49] M.-H. Richard, M. Chevallier, D. Dauvergne, N. Freud, P. Henriquet, F. Le Foulher, J. Letang, G. Montarou, C. Ray, F. Roellinghoff *et al.*, "Design guidelines for a double scattering compton camera for prompt-γ imaging during ion beam therapy: A monte carlo simulation study," *IEEE Transactions on Nuclear Science*, vol. 58, no. 1, pp. 87–94, 2010.

[50] E. Hilaire, D. Sarrut, F. Peyrin, and V. Maxim, "Proton therapy monitoring by Compton imaging: influence of the large energy spectrum of the prompt-γ radiation," *Physics in Medicine & Biology*, vol. 61, no. 8, p. 3127, 2016.

[51] E. Draeger, S. Peterson, D. Mackin, H. Chen, S. Beddar, and J. C. Polf, "Feasibility studies of a new event selection method to improve spatial resolution of compton imaging for medical applications," *IEEE transactions on radiation and plasma medical sciences*, vol. 1, no. 4, pp. 358–367, 2017.

[52] V. Maxim, X. Lojacono, E. Hilaire, J. Krimmer, E. Testa, D. Dauvergne, I. Magnin, and R. Prost, "Probabilistic models and numerical calculation of system matrix and sensitivity in list-mode MLEM 3D reconstruction of Compton camera images," *Phys. Med. Biol.*, vol. 61, no. 1, pp. 243–264, 2016.

[53] S. Schoene, W. Enghardt, F. Fiedler, C. Golnik, G. Pausch, H. Rohling, and T. Kormoll, "An image reconstruction framework and camera prototype aimed for compton imaging forin-vivodosimetry of therapeutic ion beams," *IEEE Transactions on Radiation and Plasma Medical Sciences*, vol. 1, no. 1, pp. 96–107, 2016.

[54] E. Muñoz, J. Barrio, J. Bernabéu, A. Etxebeste, C. Lacasta, G. Llosá, A. Ros, J. Roser, and J. F. Oliver, "Study and comparison of different sensitivity models for a two-plane compton camera," *Physics in Medicine & Biology*, vol. 63, no. 13, p. 135004, 2018.

[55] T. Ida, S. Motomura, M. Ueda, Y. Watanabe, and S. Enomoto, "Accurate modeling of event-by-event backprojection for a germanium semiconductor Compton camera for system response evaluation in the LM-ML-EM image reconstruction method," *Japanese Journal of Applied Physics*, vol. 58, no. 1, p. 016002, 2018.

[56] D. Xu and Z. He, "Gamma-ray energy-imaging integrated deconvolution," *Nucl Instr Meth*, vol. A574, no. 1, pp. 98–109, 2007.

[57] S. M. Kim, H. Seo, J. H. Park, C. H. Kim, C. S. Lee, S.-J. Lee, D. S. Lee, and J. S. Lee, "Resolution recovery reconstruction for a compton camera," *Physics in Medicine & Biology*, vol. 58, no. 9, p. 2823, 2013.

[58] M.-L. Jan, M.-W. Lee, and H.-M. Huang, "PSF reconstruction for Compton-based prompt gamma imaging," *Physics in Medicine & Biology*, vol. 63, no. 3, p. 035015, 2018.

[59] A. Zoglauer, R. Andritschke, and G. Kanbach, "Data analysis for the MEGA prototype," *New Astronomy Reviews*, vol. 48, no. 1-4, pp. 231–235, Feb. 2004.

[60] Y. Yang, Y. Gono, S. Motomura, S. Enomoto, and Y. Yano, "A compton camera for multitracer imaging," *IEEE Transactions on Nuclear Science*, vol. 48, no. 3, pp. 656–661, 2001.

[61] T. Kormoll, F. Fiedler, C. Golnik, K. Heidel, M. Kempe, S. Schoene, M. Sobiella, K. Zuber, and W. Enghardt, "A prototype compton camera for in-vivo dosimetry of ion beam cancer irradiation," in *2011 IEEE Nuclear Science Symposium Conference Record*. IEEE, 2011, pp. 3484–3487.

[62] G. Llosá, J. Barrio, C. Lacasta, S. Callier, C. de La Taille, and L. Raux, "Characterization of a detector head based on continuous labr 3 crystals and sipm arrays for dose monitoring in hadron therapy," in *IEEE Nuclear Science Symposium & Medical Imaging Conference*. IEEE, 2010, pp. 2148–2150.

[63] D. Robertson, J. C. Polf, S. W. Peterson, M. T. Gillin, and S. Beddar, "Material efficiency studies for a compton camera designed to measure characteristic prompt gamma rays emitted during proton beam radiotherapy," *Physics in Medicine & Biology*, vol. 56, no. 10, p. 3047, 2011.

[64] D. Sarrut, M. Bardiès, N. Boussion, N. Freud, S. Jan, J. M. Létang, G. Loudos, L. Maigne, S. Marcatili, T. Mauxion, P. Papadimitroulas, Y. Perrot, U. Pietrzyk, C. Robert, D. R. Schaart, D. Visvikis, and I. Buvat, "A review of the use and potential of the GATE Monte Carlo simulation code for radiation therapy and dosimetry applications," *Medical Physics*, vol. 41, no. 6, p. 064301, 2014.

[65] A. Etxebeste, Y. Feng, J. M. Létang, V. Maxim, É. Testa, and D. Sarrut, "An extension of the GATE Monte Carlo simulation toolkit to model Compton camera systems," in *Third Geant4 International User Conference*, 2018.

[66] L. Shepp and Y. Vardi, "Maximum likelihood reconstruction for emission tomography," *IEEE Transactions on Medical Imaging*, vol. 1, no. 2, pp. 113–122, 1982.

[67] K. Lange and R. Carson, "EM reconstruction algorithms for emission and transmission tomography," *J Comput Assist Tomogr*, vol. 8, no. 2, pp. 306–316, 1984.

[68] A. Dempster, N. Laird, and D. Rubin, "Maximum likelihood from incomplete data via the EM algorithm," *Journal of the Royal Statistical Society. Series B (Methodological)*, vol. 39, pp. 1–38, 1977.

[69] H. Hudson and R. Larkin, "Accelerated image reconstruction using ordered subsets of projection data," *IEEE transactions on medical imaging*, vol. 13, no. 4, pp. 601–609, 1994.

[70] H. H. Barrett, T. White, and L. C. Parra, "List-mode likelihood," *JOSA A*, vol. 14, no. 11, pp. 2914–2923, 1997.

[71] S. Wilderman, N. Clinthorne, J. Fessler, and W. Rogers, "List-mode maximum likelihood reconstruction of Compton scatter camera images in nuclear medicine," in *IEEE Nuclear Science Symposium*, November 1998, pp. 1716–1720.

[72] L. Rudin, S. Osher, and E. Fatemi, "Nonlinear total variation based noise removal algorithms," *Physica D: nonlinear phenomena*, vol. 60, no. 1-4, pp. 259–268, 1992.

[73] A. Chambolle, "An algorithm for total variation minimization and applications," *Journal of Mathematical imaging and vision*, vol. 20, no. 1-2, pp. 89–97, 2004.

[74] A. C. Sauve, A. O. Hero, W. L. Rogers, S. J. Wilderman, and N. H. Clinthorne, "3D image reconstruction for a Compton SPECT camera model," *IEEE Transactions in Nuclear Science*, vol. 46, no. 6, pp. 2075–2084, 1999.

[75] S. Wilderman, J. Fessler, N. Clinthorne, J. LeBlanc, and W. Rogers, "Improved modeling of system response in list mode EM reconstruction of Compton scatter camera images," *IEEE Transactions on Nuclear Science*, vol. 48, pp. 111–116, 2001.

[76] S. Tornga, M. R. Sullivan, and J. Sullivan, "Three-dimensional Compton imaging using list-mode maximum likelihood expectation maximization," *IEEE Trans. on Nuclear Science*, vol. 56, no. 3, pp. 1372–76, 2009.

[77] O. Klein and Y. Nishina, "Über die streuung von strahlung durch freie elektronen nach der neuen relativistischen quantendynamik von dirac," *Zeitschrift für Physik*, vol. 52, no. 11-12, pp. 853–868, 1929.

[78] J. Nuyts and J. A. Fessler, "A penalized-likelihood image reconstruction method for emission tomography, compared to postsmoothed maximum-likelihood with matched spatial resolution," *IEEE transactions on medical imaging*, vol. 22, no. 9, pp. 1042–1052, 2003.

[79] J. W. Stayman and J. A. Fessler, "Compensation for nonuniform resolution using penalized-likelihood reconstruction in space-variant imaging systems," *IEEE transactions on medical imaging*, vol. 23, no. 3, pp. 269–284, 2004.

[80] A. Sawatzky, C. Brune, F. Wubbeling, T. Kosters, K. Schafers, and M. Burger, "Accurate EM-TV algorithm in PET with low SNR," in *Nuclear Science Symposium Conference Record, 2008. NSS'08. IEEE*. IEEE, 2008, pp. 5133–5137.

[81] V. Maxim, Y. Feng, H. Banjak, and E. Bretin, "Tomographic reconstruction from Poisson distributed data: a fast and convergent EM-TV dual approach," INSA Lyon, https://hal.archives-ouvertes.fr/hal-01892281/, preprint, 2018.

[82] A. Beck and M. Teboulle, "A fast iterative shrinkage-thresholding algorithm for linear inverse problems," *SIAM journal on imaging sciences*, vol. 2, no. 1, pp. 183–202, 2009.

[83] Z. Wang, A. C. Bovik, H. R. Sheikh, E. P. Simoncelli *et al.*, "Image quality assessment: from error visibility to structural similarity," *IEEE transactions on image processing*, vol. 13, no. 4, pp. 600–612, 2004.

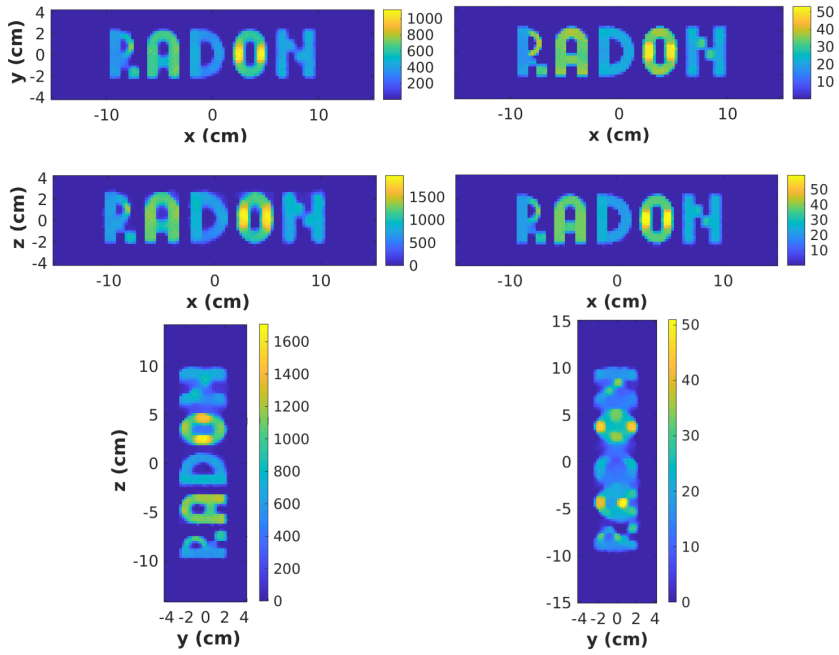

(a) Compton camera (b) Missing angle Anger camera

Fig. 7. Images reconstructed from Compton camera (left) and missing angle Anger camera (right), as a function of source position. Form the top to the bottom the sources placement corresponds to the configuration denoted respectively as (C1), (C2) and (C3) in figure 3. Central cuts are shown at the 200th iteration of the TV-MAP-EM algorithm applied at 2×10^6 measured events.

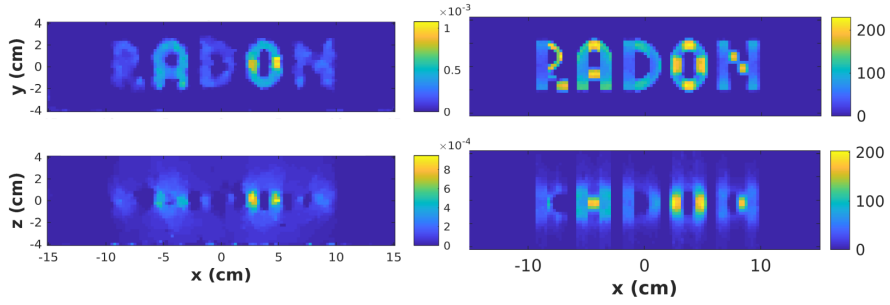

(a) Compton analytic reconstruction (b) Anger analytic reconstruction

Fig. 8. Filtered backprojection reconstruction from Compton camera and from missing angle collimated camera data. Total variation denoising was applied to the reconstructed volumes.